

A Novel Rotor Topology for High-Performance Fractional Slot Concentrated Winding Interior Permanent Magnet Machine

Rukmi Dutta^{ID}, Senior Member, IEEE, Alireza Pouramin^{ID}, and Muhammed F. Rahman^{ID}, Life Fellow, IEEE

Abstract—This article presents a finite-element-based, multiobjective design optimization study of the fractional-slot, concentrated wound, permanent magnet synchronous machine (FSCW PMSM). Design objectives included maximization of efficiency, minimization of cost and low ripple without sacrificing torque density and wide constant power speed range. A large-scale optimization study revealed that while a V-type rotor provides high torque density, a spoke-type rotor has the benefit of low torque ripple. Quest for a design that can combine the goodness of both V- and spoke type rotors for an FSCW stator has led to a novel interior permanent magnet rotor topology referred here as Y-type. The goals of achieving maximum efficiency, minimum cost and wide CPSR were also accomplished in the proposed Y-type FSCW IPMSM. For experimental verification purpose, three fully optimized rotors - V-, spoke- and Y-type were constructed for a 12-slot/10-pole FSCW stator. Extensive experimental tests were conducted on three machines for a detailed comparison study. It will be shown that the proposed Y-type FSCW IPMSM outperforms both V and spoke-type configurations. A scaled-up version of the Y-type FSCW IPMSM shown to have satisfied many of the Freedomcar 2020 targets, which is promising for application in electric vehicles.

Index Terms—Fractional slot, concentrated winding, interior permanent magnet machine, electric machine, PMSM, IPMSM.

I. INTRODUCTION

IT IS common knowledge that nearly half of the world's electrical energy is consumed by the industrial motor-drive system [2]. For sustainable industrial growth, many standards such as the national electrical manufacturers association (NEMA), the international electrotechnical commission (IEC) and energy policy act (EPAct) have recommended enhanced performances for electrical machines. Among many factors that define high performances of an electrical machine, high efficiency, low torque ripple, high torque density, high power factor, fast dynamics, mechanical robustness are considered as of significant importance. The permanent magnet synchronous machines (PMSMs)

Manuscript received November 22, 2019; revised April 28, 2020 and August 20, 2020; accepted October 3, 2020. Date of publication October 13, 2020; date of current version May 21, 2021. This work was supported by the Australian Research Councils (ARC) Discovery Project DP130103760. Paper no. TEC-01133-2019. (Corresponding author: Rukmi Dutta.)

The authors are with the UNSW, Sydney, NSW 2052, Australia (e-mail: rukmi.dutta@unsw.edu.au; pouramin@gmail.com; f.rahman@unsw.edu.au).

Color versions of one or more of the figures in this article are available online at <https://ieeexplore.ieee.org>.

Digital Object Identifier 10.1109/TEC.2020.3030302

demonstrate higher performance in terms of many of these factors and hence, a preferred choice for applications such as an electric vehicle. In recent times, the PMSMs with fractional-slot concentrated-winding (FSCW) stator has gained attention from the research community because of easy manufacturability, wide constant power speed range (CPSR), high torque/power density, low torque ripple and weak mutual coupling between phases for higher fault tolerance [3]–[6].

The FSCW, being a relatively new entrant, a global optimum rotor topology especially suitable for FSCW stator is yet to find. In recent times, several studies were carried out to further improve performances of the FSCW PMSMs [7], [8]. Use of consequent pole rotor with FSCW stator for the low-speed application was studied in [7]. In [8], an investigation was carried out to adopt unconventional slot-pole combinations using multilayer structure in an FSCW stator.

A comparative study between surface-type and interior-type rotors with FSCW stator was carried out in [9] and concluded that eddy current loss of the rotor magnet is lower in the interior-type rotor.

The multiobjective optimization in machine design is gaining attention. For example, in [10], a rotor-shaping multiobjective optimization method was proposed to reduce mechanical stress and weight of a surface-type PMSM. The reference [11] uses supervised machine learning technique to optimized a consequent pole, six-phase PMSM to achieve high torque density with low torque ripple for an EV application. A highly sophisticated dual-level response surface optimization technique was employed in [12] to maximize power while minimizing the cost of direct-drive, surface-type PM synchronous generator.

The design space of an FSCW interior permanent magnet synchronous machine (IPMSM) is much broader than distributed winding surface-type PMSM due to vast possibilities of slot-pole configuration combined with a wide range of interior-type permanent magnet (IPM) rotor topologies considering shape, size, the arrangement of magnets and flux barriers. Various design studies [5], [13]–[16] have independently investigated the performance of commonly found IPM rotor topologies with FSCW stator. However, very few studies have compared performances of these rotor topologies to find the most compatible one that improves several performances concurrently. In more recent times, several studies [3], [17]–[22] were conducted to enhance only specific performances of the FSCW IPMSM while other performance aspects were either compromised or ignored.

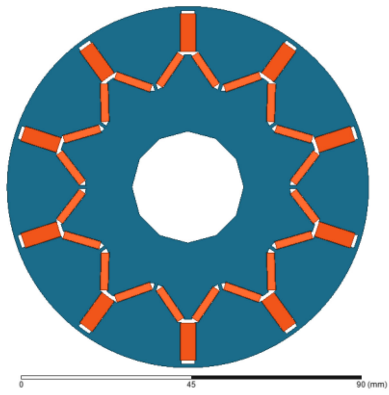


Fig. 1. Cross-section of a novel Y-type rotor topology.

For example, [23] investigated methods to reduce the MMF harmonics and the torque ripple caused by these harmonics while compromising the torque density. On the contrary, [22] proposed a method to increase torque density without considering an increase in torque ripple or losses. The reference [24] used a multiobjective stratified optimization technique to reduce rare-earth material in a 12-slot/10-pole FSCW IPMSM. The resulted rotor topology combined spoke-type and V-type structure where the spoke-type section was made with ferrite magnet.

In this paper, a systematic multiobjective finite element (FE)-based optimization procedure was first established to explore the vast design space of FSCW IPMSMs considering various feasible slot-pole combinations and several different IPM rotor topologies found in the literature [25]. The objectives of the optimization were to find the optimum FSCW IPMSM design candidates that can meet the design targets of maximum efficiency and torque density with minimum cost and torque ripple without compromising the wide constant power speed range (CPSR). Although, the V- and spoke-type topologies for a 10-pole/12-slot FSCW stator stood out as the superior candidates, neither could satisfy the targets of torque ripple and torque density concurrently. The V-type topology provides excellent torque density but compromises on torque ripple. In contrast, the spoke-type minimizes torque ripple significantly, but torque density is lower than that of a V-type FSCW IPMSM. Thus, both topologies require a compromise of one or other performance criteria. These findings suggested that if the features of both V- and spoke-type can be combined into a novel rotor topology, an optimum FSCW IPMSM can be arrived at which satisfies the design targets. The proposed novel rotor topology uses an inverted Y-shape magnet arrangement per pole and will be referred to as Y-type rotor from here onward. A close inspection of the Y-type rotor of Fig. 1 shows that it comprises of a spoke magnets section and a V-section. The spoke section reduces the torque ripple while V-section increases the torque density. As a result, the Y-type rotor simultaneously increases torque density and decrease the torque ripple, which cannot be achieved in other rotor topologies. It should be noted that unlike [24], the proposed Y-type rotor uses only rare-earth material and the spoke-section is closer to the airgap instead of V-section as in [24].

It will be shown via experimental results that the proposed Y-type rotor enhances the critical performance aspects of FSCW

IPMSM considered for optimization without sacrificing any of the major performance aspects while maintaining lower material cost than the other two topologies. The Y-type rotor has additional design freedom. For example, if the torque density is the design priority, then the V-section can be made larger than the spoke-section in the Y-type rotor. A well-defined parametric FE model of the Y-type rotor can smoothly vary the topology between a V-type, spoke-type and any combination of them.

The development of the proposed optimization algorithm leading to the proposal of the Y-type rotor topology stemmed from meeting the Freedomcar 2020 targets detailed in [26]. Hence, the proof-of-concept prototype was scaled-up to 30kW continuous power rating for further study. It was found that the scaled-up motor is able to satisfy many of the challenging targets such as peak torque, torque and back EMF at the maximum speed required for application in the electric vehicle.

The paper is arranged as follows: after the introduction in Section I, Section II briefly discusses key theoretical design aspects of an FSCW IPMSM. Section III describes the multiobjective optimization method developed for optimization of FSCW IPMSMs. Section IV describes the selection process of the optimized sizing of the FSCW IPMSM. Section V discusses the optimization results and the development of the novel Y-type rotor topology. Three optimized FSCW IPMSM were constructed and tested experimentally for the entire range of operations. The experimental results are presented in Section VI, and the concluding remarks are provided in Section VII.

II. DESIGN ASPECTS OF FSCW IPMS

Fractional-slot, concentrated windings (FSCWs) refer to a subclass of AC windings for which slot per pole per phase (S_{pp}) is a proper fraction. An alternative classification is also used in the literature as tooth-coil or non-overlapping winding because the coils of an FSCW are concentrated around a single tooth and do not overlap with other phases at the end-windings. Compared to conventional distributed winding, the FSCW produces non-sinusoidal MMF (magneto-motive force) and an only particular combination of slot and pole results in >0.9 winding factor.

Bianchi *et al.* in [27], [28] and El-Refaie in [5], [28] summarized the majority of the research carried out in the design and analysis of FSCW PMSMs in recent years. The key aspects that arose from these studies are:

- 1) a large least common multiple (LCM) between the number of poles and the number of slots minimizes cogging torque,
- 2) copper loss reduces because of short end-winding and hence, allows the shorter total axial length of the machine,
- 3) due to the presence of sub- and high order MMF harmonics machine inductances increases allowing characteristic current (ratio of magnet flux linkage to d -axis inductance) to be equal to rated current for wider CPSR,
- 4) fault-tolerant capability is better because of low mutual inductance, and
- 5) additional MMF harmonics causes unwanted eddy current loss in the rotor and magnet.

FSCWs can be further classified according to the number of layers in the slots as, single-layer, double-layer, or multilayer windings. Fig. 2 shows the difference between the single and

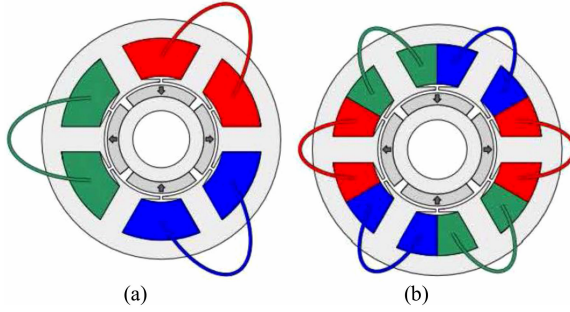


Fig. 2. (a) single-layer FSCW and (b) double-layer FSCW stator [1].

double layer FSCW of a 3-phase 4-pole/6-slot surface type PM machine [1]. The single-layer windings are thermally and electrically isolated with very low mutual inductance and hence, preferable for fault-tolerant applications. The double-layer FSCW has lower MMF harmonics than single layer resulting in lower core losses. Other multilayer windings are also proposed to eliminate MMF subharmonics to reduce core losses, but they increase manufacturing complexity and reduce fault tolerance. It was shown in [29]–[32] that the double layer FSCW is a good compromise in terms of MMF harmonics, fault tolerance, complexity and performances. Therefore, in this paper, only double layer FSCW was considered in the optimization study.

A. Common Slot-Pole Combinations

In an FSCW PM machine, not all combinations of slots and poles yield acceptable performances. The slot and pole combinations are selected based on maximum possible main winding factor k_w and minimum possible cogging torque, torque ripple, vibration, and losses.

Generally, the winding function and the optimal winding layout are determined by using any one of three well-known methods – star-of-slot method, closed-form expression and winding function theory. However, a slot-pole combination that gives high k_w does not always result in the symmetrical winding. The winding asymmetry is the main cause of unbalanced magnetic pull that produces vibration and noise in an electric machine. It was shown in [18] that symmetrical winding results when (1) is satisfied.

$$\frac{Q}{\text{GCD}\{Q, P\}} = mk \quad (1)$$

where, Q : slot numbers, P : pole numbers, m : phase number and k : an integer.

The greatest common divisor (GCD) of slot and pole number also defines the electrical periodicity of an FSCW machine. The minimum possible slot and pole number of satisfying (1) are defined as a base set, which can be used to find the slot per pole per phase S_{pp} as follows,

$$S_{pp} = \frac{Q_{\text{base}}}{m \times P_{\text{base}}} \quad (2)$$

It was shown in [28] that peak of the cogging torque reduces when the lowest common multiple (LCM) of slot and pole

TABLE I
DIFFERENT CATEGORIES OF THE MOST COMMON DOUBLE-LAYER FSCW STATORS

Category	S_{pp}	$k_w, (P/2)$	Frequently reported combinations
A	$1/(3k \pm 1)$, $k = 1, 3, 5, \dots$	0.866	12slot/8pole, $S_{pp};1/2$
B	$1/(3k \pm 1)$, $k = 2, 4, 6, \dots$	0.5	N/A
C	$2/(6k \pm 1)$, $k = 1, 3, 5, \dots$	0.933	12slot/10 pole, $S_{pp};2/5$ 12slot/14pole, $S_{pp};2/7$
D	$3/(9k \pm 2)$, $k = 1, 3, 5, \dots$	0.902	18slot/14pole, $S_{pp};3/7$
E	$3/(9k \pm 1)$, $k = 1, 3, 5, \dots$	0.945	18slot/16pole, $S_{pp};3/8$

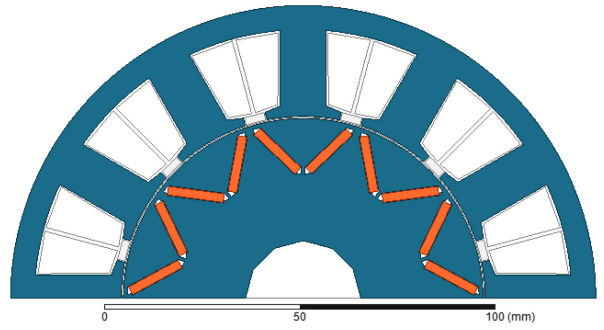


Fig. 3. Winding arrangement of 12-slot 10-pole, FSCW stator.

number is high. Therefore, high LCM of slot-pole combination is also a selection criterion along with the high k_w .

The MMF spatial harmonics are the leading cause of rotor core loss. It is useful to categorize the slot and pole combinations that result in the same spatial MMF harmonics into one single category [27]. Moreover, odd pole pairs of the configuration, makes it also better fault-tolerant due to smaller mutual inductance than the even pole pair ones such as 18slot/16pole [33].

Table I lists such categories and includes the most frequently reported slot/pole combination of each category. Many applications such as electric vehicles (EVs), general-purpose motors, and electric pumps prefers the low number of poles, so to have a high base speed at a defined frequency. Besides, the low number of poles allow operation at relatively low supply frequencies which decreases the losses in the drive system. The minimum slot/pole combination to produce a main winding factor $k_w > 0.9$ is 12 slot/10 pole, and hence, it is the preferred choice for many high-performance applications including EVs. Moreover, odd pole pairs of the configuration, makes it also better fault-tolerant due to smaller mutual inductance than the even pole pair ones such as 18 slot/16 pole [33].

The optimum winding layout of double-layer FSCW PMMSM is well-established in the literature [5], [6], [34], [35] and hence, it will not be discussed further. The double-layer optimal winding arrangement of 12slot/10pole FSCW stator shown in Fig. 3 was adopted in the paper.

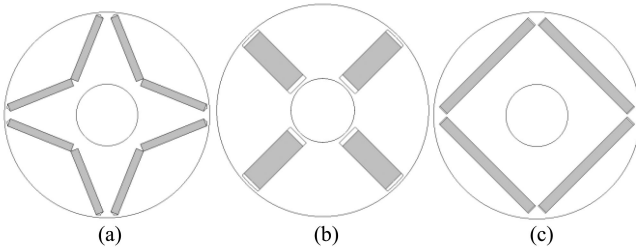


Fig. 4. Common IPM rotor topologies (a) V-type, (b) Spoke-type, and (c) Flat-type.

B. Common Interior Permanent Magnet Rotor Topologies

In an interior type permanent magnet rotor, the pole magnets are buried in the rotor iron core, and usually, flux barriers are provided for flux concentration. Due to the freedom to select positions, shapes and dimensions of pole magnet and flux barriers, many different rotor topologies were realized. The three most used IPM rotor topologies are shown in Fig. 4. For FSCW stator, V-shaped and spoke type are found to be more favorable in terms of flux concentration than the flat-type. A large optimization study carried out in [25] concluded that torque density and torque per magnet usages are higher in a V-type FSCW IPMSM than other types. It also has higher efficiency, saliency ratio and current angle (i.e. a more substantial reluctance torque component) than other types. In the same study, it was found that spoke type rotor with FSCW stator produces the lowest torque ripple. Therefore, in this paper, V- and spoke-type rotors were considered for the further optimization study.

III. A MULTIOBJECTIVE OPTIMIZATION METHOD FOR FSCW IPMSMs

The design space of the FSCW IPMSM is much wider due to the possibility of combinations of different slot-pole and rotor topologies. Even if the design studies are restricted to common slot-pole and rotor topologies, there still considerable freedom of choice exists. Moreover, the presence of non-negligible MMF harmonics and, leakage flux at the narrow iron bridges make analytical method impractical for large-scale design optimization studies. Therefore, a computationally efficient finite element analysis (CE-FEA) based design optimization method was considered in this study. In general, in a design optimization process, an initial population is selected randomly, which is then evaluated by the objective functions. An iterative process searches for the optimum designs. New population for each iteration is selected using a defined search criterion. Various design constraints usually set the boundary of the search space. Stochastic search algorithms are preferable in design optimization because of their ability to overcome local optima and to include multiobjective functions. Among many Stochastic algorithms, Nondominated Sorting Genetic Algorithm (NSGA-II) produces the desired results with the least time when the design variables are limited and well-defined as demonstrated in [34]. The detailed development of NSGA-II and its application to FE-based optimization can be found in [35]–[37]. The FSCW

TABLE II
GEOMETRIC PARAMETERS AND DESIGN VARIABLES (**BOLD**)

Parameter	Description
n_s	Number of stator slot
D_o	Stator outer diameter
D_i	Stator inner diameter
g	Length of the airgap
TWS	Tooth width
Yk	Depth of yoke
S_o	Slot opening width
S_{sh}	Slot opening height
P	Number of rotor poles
m_h	Magnet thickness
m_w	Magnet width
k_{mw}	Ratio between magnet width and rotor yoke
w_{th}	Width of iron rib
b_{th}	Thickness the iron bridge
s_g	Thickness of the middle iron bridges
m_z	Clearances between magnets and rotor slots

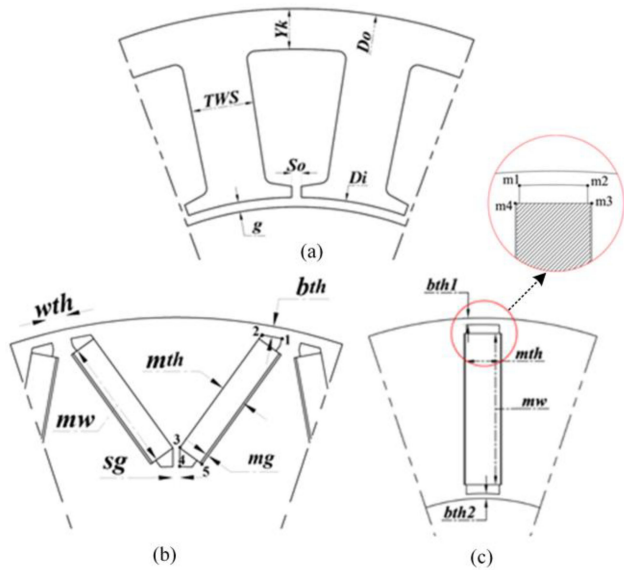


Fig. 5. The cross-section and geometric parameters of (a) 1-slot pitch and 1-pole pitch of (b) V-type and (c) spoke type rotors.

IPMSM considered in the study has well-defined design variables of less than 10, which are tightly bound by the physical limits. Hence, NSGA-II was deemed to be appropriate for this study.

The geometric parameters of the stator and the rotors described in Table II can be identified in Fig. 5. Among these parameters, only those which are independent of each are selected as the design variables. These are shown with the bold letters in Table II. In this study, the outer diameter D_o was fixed by the chosen frame size and hence, excluded as a design variable. By defining the xy coordinate positions in terms of design variables, a parameterized FE model was prepared for optimization. The upper and lower bounds of the design variables were selected appropriately not to violate practical feasibility.

TABLE III
DESIGN CONSTRAINTS

Constraints	Boundary
Torque ripple	< 5%
Saliency ratio	> 1.3
characteristic current (I_{ch})	$0.95 \leq I_{ch} \leq 1.05$
Demagnetization B_{pm}	$\geq 0.3B_r$
THD (induced Voltage)	< 5%
Average flux density at stator teeth B_{teeth}	< 1.6 T
Average flux density at stator yoke B_{yoke}	< 1.5 T

A. Design Objectives and Constraints

The efficiency and material cost were selected as two design objectives. The maximization of efficiency was performed using to (3) – (5) and minimization of the cost was calculated using (6).

$$\eta = \frac{P_{out}}{P_{in}} = \frac{T_e \omega_m - P_{Loss}}{T_e \omega_m + P_{Cu}} \quad (3)$$

where, T_e : induced electromagnetic torque and ω_m : rotational speed. The total loss P_{Loss} is calculated according to (4).

$$P_{Loss} = P_{Cu} + P_{Coreloss} + P_{PMloss} + P_{mech} \quad (4)$$

where, P_{cu} : copper loss, $P_{Coreloss}$: stator and rotor core loss, P_{PMloss} : magnet losses, P_{mech} : mechanical losses.

The copper loss P_{cu} was estimated using the following expression,

$$P_{Cu} = m I_{rms}^2 \left(\frac{r_c^2}{2r_c \delta_{skin} - \delta_{skin}^2} \right) \left(\frac{1}{a} \rho_{Cu} \frac{L_{coil}}{A_{Cu}} \right) \quad (5)$$

where, m : number of phases, I_{rms} : rms phase current, r_c : conductor radius, a : parallel current paths, L_{coil} : total length of the conductor, ρ_{cu} : resistivity of copper at 20C, A_{cu} cross-sectional area of the conductor and δ_{skin} : skin depth, which is a function of electrical angular frequency and permeability of copper. Thus, the equation (5) estimates copper losses considering both AC and DC resistances.

The cost of the active materials was estimated as follows:

$$\text{Active material cost} = c_{pm} w_{pm} + c_{Cu} w_{Cu} + c_{Fe} w_{Fe}, \quad (6)$$

where, w_{pm} , w_{Cu} and w_{Fe} are the masses of the magnet, copper, and laminated steel, respectively. In (6) c_{pm} , c_{Cu} , and c_{Fe} , are the price coefficients of magnets (sintered NdFeB), copper and lamination steel, respectively. These coefficients were selected based on the market values at the time of this work, and given as $c_{pm} = 26 \text{ \$/kg}$, $c_{Cu} = 3 \text{ \$/kg}$ and $c_{Fe} = 1 \text{ \$/kg}$. Cost of steel was considered as the base price for the per-unit normalization.

The torque ripple defined as (7) is used to estimate the value.

$$T_{\text{ripple}} = \frac{\max(T_{\text{mech}}) - \min(T_{\text{mech}})}{T_{\text{mech}}} \times 100 \quad (7)$$

Torque ripple, along with all other key performance criteria was set as design constraints and the boundary values were provided in Table III.

B. Transient CE-FEA

Use of FEA in a stochastic-based optimization is numerically demanding. Therefore, it is essential to make the process as computationally efficient as possible. The computationally efficient FE (CE-FE) discussed in [38], [39] uses electrical symmetry, magnetic periodicity of PMSM and magnetostatics FEA combined with analytical models to reduce the computational burden. However, further considerations are required to use the CE-FE of [38], [39]. The magnetostatics-based CE-FE is unable to estimate rotor losses during the optimization. The CE-FE was modified in this study to use transient instead of magnetostatics FEA combined analytical models.

Thus, the evaluation of the cost functions was carried out using the transient- CE-FEA method, which took the help of transient FEA solver of ANSYS Maxwell. ANSYS Maxwell allows dynamic meshing by varying the size of the mesh element with respect to geometry. In dynamic meshing, size and density are controlled by a mesh factor. Larger is the mesh factor the finer and smaller are the mesh density and size. The mesh size and densities were determined following the general rule, i.e. high mesh density in the operation-critical regions such as the air gap and its surrounding areas, thin iron bridges around the magnets, and slot openings. Once an optimum mesh density was found based on the accuracy of the expected results, it was kept unchanged for the design candidates during the optimization. Furthermore, for optimization of saliency ratio, characteristic current and operating points of maximum torque per ampere (MTPA) trajectory under non-linear magnetic saturation, using transient CE-FEA require additional considerations. The effect of saturation on the saliency ratio was included by calculating the inductance matrix in FEA from the stored energy obtained under frozen permeability. Accuracy and capability of this method were discussed in [40] and will not be repeated here.

C. Estimation of Characteristic Current

Characteristic current I_{ch} , is defined as the ratio of magnet flux linkage λ_{pmd} , to d -axis inductance L_d . If I_{ch} is equal to the rated current (i.e. 1 pu), the CPSR extends theoretically to infinity [41]. To design IPM machines with wide CPSR, I_{ch} can be considered as an objective function or as a constraint during a design optimization process. Hence, an accurate estimation of I_{ch} during design optimization is required. If λ_{pmd} and L_d are obtained from a frozen permeability FEA using $i_d = 0$ and $i_q = 1 \text{ pu}$, it will not correspond to the actual operating point, i.e. $i_d = -I_{ch}$ and $i_q = 0$. To estimate characteristic current, λ_{pmd} and L_d should be obtained as:

$$\lambda_{pmd}^{ch} = \lambda_{pmd}(-I_{ch}, 0) \quad (8)$$

and

$$L_d^{ch} = \frac{\lambda_d(-I_{ch}, 0) - \lambda_{pmd}(-I_{ch}, 0)}{-I_{ch}} \quad (9)$$

Since λ_{pmd}^{ch} and L_d^{ch} are a function of I_{ch} , the use of them to determine I_{ch} will result in a nested loop. To avoid such a condition I_{ch} can be determined using its fundamental definition, i.e. I_{ch} is a negative i_d current to make the resultant d -axis flux λ_d

zero. The λ_d is a function of i_d which can be obtained from FEA. $\lambda_d(i_d) = 0$, when $i_d = -I_{ch}$. Therefore, I_{ch} can be calculated by solving the equation $\lambda_d(i_d) = 0$ for a negative i_d value. However, implementation of the proposed method of calculating I_{ch} during the optimization is not straightforward. Stochastic-based design optimization process uses a random procedure to select the design candidates of the next generation. Due to the randomness, it is possible to have design candidates with $I_{ch} << 1$ pu or $I_{ch} >> 1$ pu. Therefore, estimation of I_{ch} during the optimization requires many samples and increases computational time significantly. The following steps are proposed to reduce the number of samples:

First, an approximation value I'_{ch} was obtained under the full load condition. Then two values around I'_{ch} were selected as $I_d = -I'_{ch} \pm \Delta I_d$ and the two values $\lambda_d(-I'_{ch} \pm \Delta I_d)$ were obtained from FEA. It is assumed that if $\pm \Delta I_d$ is small, the variation of $\lambda_d(i_d)$ at the vicinity of I'_{ch} is linear. Hence, using a linear curve fitting of data points, the function $\lambda_d(i_d)$ can be estimated. Once, $\lambda_d(i_d)$ is found, by equating it to zero, an easily solvable linear equation $\lambda_d(i_d) = 0$ is obtained, and the solution of this equation gives the final value of I_{ch} . The procedure was implemented as an online routine during optimization.

D. MTPA Trajectory Estimation

In the constant torque region, the electromagnetic behavior of the IPM machines is typically evaluated at the MTPA trajectory, which necessitates an accurate method for the estimation of the MTPA trajectory in the electromagnetic design optimization of IPM machines. Estimation of the MTPA trajectory for IPM machines is a complex task as it occurs in the second quadrant of the dq plane due to the presence of reluctance torque. Accurate MTPA trajectory estimation is possible using detailed FEA. However, this will increase the computational time by several orders of magnitude even when advanced computational resources with high processing power are used. Therefore, conventionally, the MTPA trajectory during the design optimization is found by calculating electromagnetic torque from the classical dq equation using the constant value of the machine parameters. The optimum current vector to produce the maximum torque is then used for further processing of design optimization. The combination of the classical dq model and CE-FEA was used to estimate the MTPA operating point during the design optimization in [39], [42]. This method is computationally fast as it only requires three FEA runs in the pre-processing stage of the design optimization procedure [43]. However, the accuracy of the estimated MTPA trajectory suffers greatly if the effect of saturation is high. The pre-calculated torque from the dq equation ignores any variation of inductances and the magnet flux linkage due to saturation. In [44], the authors proposed a model to estimate the operating points for both constant torque and power operations using look-up tables of flux linkages obtained via magnetostatics FEA. This method includes the effect of saturation, but pre-calculation of flux linkages for the look-up table increases the computational time as it requires a significant number of FEA runs for each design candidate during the optimization process. In this paper, a transient FEA-based online-search process is developed to reduce the computational

```

Discrete-search algorithm
for MTPA trajectory
for  $\gamma=[0, 20, 40, 60]$ 
  for  $I=[0.5pu, 1pu]$ 
    get  $T_{dev}(I, \gamma)$ 
  end
end
set  $T_{dev}(I=0, \gamma=[0:90])=0$ 
set  $T_{dev}(I=0.5pu, \gamma=90)=0$ 
set  $T_{dev}(I=1pu, \gamma=90)=0$ 
Surf = fit surface on [I,  $\gamma$ ,  $T_{dev}$ ]
 $\gamma_{max} = \max(Surf)$ 

```

Fig. 6. The algorithm for the proposed discrete search algorithm for MTPA.

time without compromising accuracy due to saturation. In this method, a discrete-search algorithm efficiently creates a torque matrix on the $T_{dev}-\gamma$ plane with a minimum number of FEA runs. The γ is the current angle (i.e. phase angle between EMF and the current phasor). The algorithm is described as a flowchart in Fig. 6. An example can explain the reduction of computational time – when two current levels (say 0.5 pu and 1 pu) and four current angles (say from 0 to 60°) are considered, resulting in eight sampling points, and eight FEA runs for each design candidate. If the conditions of zero developed torque when current I is zero and/or when γ is 90° are also included, there will be another seven sampling points of zero torque in the torque matrix. By fitting a surface on the torque matrix, a set of γ_{max} can be obtained which gives the position of MTPA trajectory in the $T_{dev}-\gamma$ plane for various torque and current values. The discrete-search algorithm is implemented in the transient FEA using an online control program, which dynamically adjusts the FEA parameters and controls the transient simulation [45]. It was found that there is about 5% discrepancy between the estimated MTPA of the proposed discrete-search algorithm and that of the detailed FEA calculation.

E. Estimation of Losses

Another critical calculation during optimization is the efficiency for which it is crucial to calculate the losses accurately in the FEA.

Among the losses defined in (4), calculation of core and magnet losses require time-varying flux density distribution and hence, magnetostatics-based CE-FEA cannot calculate them directly. In this study, since the transient solver-based CE-FEA was used, the core and the magnet losses were calculated directly in each time step. In each time step, the volume density of the instantaneous core loss in each mesh element was found as:

$$dP_C = k_{st} \left[\underbrace{k_h B_m^2 f}_{\text{Hysteresis losses}} + \underbrace{\frac{\pi^2 \sigma d^2}{6} (B_m f)^2}_{\text{Classical losses}} + \underbrace{k_e (B_m f)^{3/2} \cdot 8.67}_{\text{Excess losses}} \right] \quad (10)$$

where, k_h : the coefficient of losses by hysteresis, k_e : the coefficient of losses in excess, σ : the conductivity of the material, d : the thickness of the lamination, f : the frequency, B_m : the peak value of the airgap flux density and k_{st} : the stack-length factor to include the effect of insulation between laminations. The total core loss at time t_1 can be calculated as:

$$P_c = \iint_{\text{Cross section}} dP_c dS \quad (11)$$

This method utilizes the value of the magnetic flux density in each mesh element, and hence, the distribution of magnetic flux density is considered. Since the core loss is calculated in each time step, the space harmonics of the magnetic field is also included. With the assumption of sinusoidal current, the average value of core loss in one-sixth of the electrical cycle can be taken as the core losses of the machine. Like the core loss calculation, the magnet loss can also be calculated directly in the transient FEA by considering the magnet as a conductive solid object.

F. Multiobjective Optimization and Computational Time

The multiobjective optimization process used in this paper has three major interfaces- a user interface, an FEA interface and an NSGA-II interface. The user interface provides input data to the FEA interface for creating a parametric model. The FEA interface evaluates design objectives using a transient FEA solver and a post-processing procedure. The design objectives and constraints are applied in the NSGA-II interface for multiobjective optimization. Interactions among the interfaces are iterative, which continues until globally optimized designs are found. Fig. 7 describes the optimization algorithm in a simplified flowchart. The python script was used as the main communication language to execute various commands and automate the optimization process.

It should be noted that the transient FEA interface of the optimization process of this study is different from the conventional transient FEA of commonly used FE software. In the transient FEA of commercial software, the user-defined time step remains constant during a simulation, and the variables change as a function of time. On the contrary, the transient FEA interface of this study uses an online control program to control the machine's parameters and variables for each time step according to the results obtained in the previous time steps. At $t = 0$, the online control program calls subroutine of MTPA trajectory estimation. The output of this subroutine is γ_{\max} , which is the input of the next time interval. In the next time interval, the inductances and saliency ratio are estimated, and the performances are evaluated at the MTPA trajectory using CE-FEA. After this, the subroutine to estimate the characteristic current is called for. In the end, based on the voltage and current limitations, the flux-weakening trajectory is estimated to evaluate the constant power speed range of each design candidate.

Python scripts were also used to export the results of the transient FEA as a set of reports for post-processing. The design objectives and constraints are employed in the NSGA-II interface to find the Pareto-front of the candidates. It should be

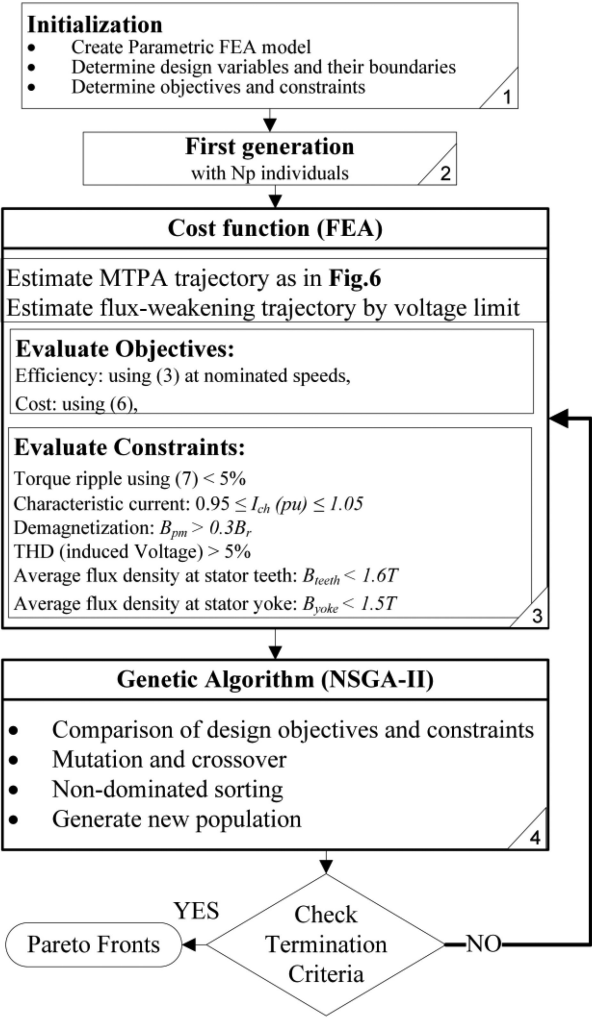


Fig. 7. The flowchart of the optimization method.

noted that all the candidates have the same developed torque for a fair comparison during the design optimization process.

The overall computational time for the full optimization depends on the rate of convergence of the objectives towards the target values and the selected size of the population. The use of transient CE-FEA and the proposed subroutines to estimate characteristic current and MTPA trajectory during the optimization process has reduced the overall computational time significantly. For example, the proposed estimation of MTPA subroutine reduces the computational time to just 9 hours from 228 hours required by the detailed FEA.

IV. OPTIMAL SIZING OF THE PROPOSED IPMSM

This section describes the procedure to explore the design space of the FSCW IPMSMs using the aforementioned optimization method. At first, a large-scale design optimization was conducted by considering the most common slot and pole combinations of S_{pp} 2/5, 2/7 and 3/7 in combination with well-known IPM rotor topologies – V-type, double-layer V-type, flat-type, double-layer flat-type, and spoke-type resulting in 15

TABLE IV
DESIGN SPECIFICATIONS

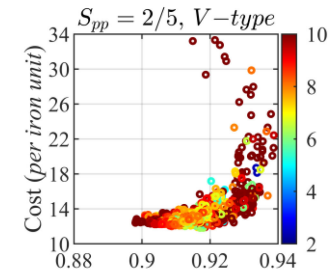
Parameter	Specification
Rated condition	1kW at 1370 rpm
Slot number, n_s	12
Pole number, P	10
Outer diameter, D_o	152 mm (IEC100)
Airgap, g	0.6 mm
s_{oh}	2 mm
Iron bridge, B_{th}	1 mm
Slot fill factor	0.48
Current density	5.7 A/mm ²
PM material	NdFeB 35EH
Electrical Steel	M400 -50A
Cooling System	Natural
Temperature	100°C (worst case)
Analysis	MTPA + FW @ 3000 rpm @ 5000 rpm
NSGA-II	Setting
N_p	100
Max iteration	50
Mutation rate	0.02

different configurations. An extensive comparison study among these configurations was carried to find candidates with the highest torque density and efficiency with the lowest torque ripple and material cost. It was found that V- and spoke-types rotors with a slot-pole combination in S_{pp} 2/5 outshine all other configurations. Therefore, only these two rotor topologies were considered in 10-pole/12-slot (S_{pp} 2/5) combination for further investigation, which has led to the development of the new Y-type rotor topology. It should be noted that the study was limited to the conventional uniform circular perimeter rotor only. No eccentric rounding of the rotor was considered in the optimization since targeted torque ripple reduction was achieved without such considerations. Besides, the conventional round rotor and uniform airgap are preferable for ease of manufacturing in machines with small airgap length.

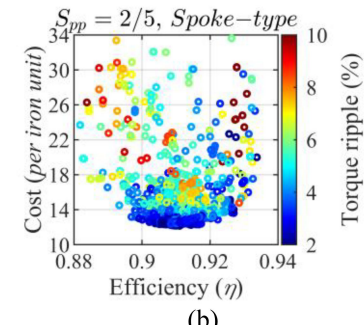
The outer diameter was fixed as 152 mm corresponding to frame size IEC100. The air gap length g , slot opening height s_{oh} , and thickness of iron bridges b_{th} are kept the same for all design cases. The effective stack length of each design candidate was scaled to achieve the same nominal torque and output power at the rated speed. The nominal torque was calculated for the given current density considering MTPA operation. With these considerations, the multiobjective design optimization was performed to find the Pareto-front of the designs. Table IV summarizes the key specifications used in design optimization.

V. OPTIMIZATION RESULTS AND NOVEL Y-TYPE ROTOR

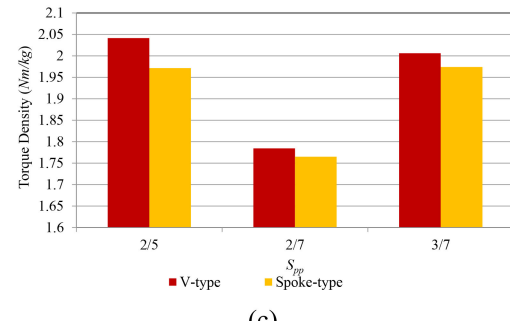
The key results of the optimization were presented in Fig. 8, which consist of 4392 candidates corresponding to 50 iterations and the population size of 80. For a fair comparison, all three rotor topologies were optimized for the same FSCW stator, material, stack length, stator and rotor diameters, air gap length, and magnet volume. The stator geometry was carefully selected from a larger optimization study which ensures that the selected stator is not biased towards any of the studied rotors.



(a)



(b)



(c)

Fig. 8. Comparison of cost, efficiency and torque ripple (a) V-type, (b) spoke-type and (c) comparison of torque density between V and spoke-type of optimized design candidates of three different slot-pole combinations.

A close observation of the candidates at the Pareto front of Fig. 8(a) and (b) indicates that for the same value of cost and efficiency, torque ripple of spoke-type designs is in range of 4-2% compared 8-10% of the V-type. Fig. 8(c) compares the torque densities of the two designs for three different S_{pp} , and V-type design has higher torque density for all three cases. Designs selected for the torque density comparison in Fig. 8(c) were determined using a post-optimization selection criterion, which would be described in detail at the later part of this section. However, neither design achieved targeted high torque density and low torque ripple simultaneously. From these comparisons, one can conclude that the spoke-type design can lower torque ripple and V-type can deliver high torque density by providing better flux concentration.

Also, if the width of the spoke-section is twice the size of the magnets in V-sections and spoke-section is nearer to the air gap, the airgap flux density will improve further. Consequently, it can be hypothesized that by combining the spoke and V-type, in the shape of an inverted Y as shown in Fig. 1, a novel rotor topology

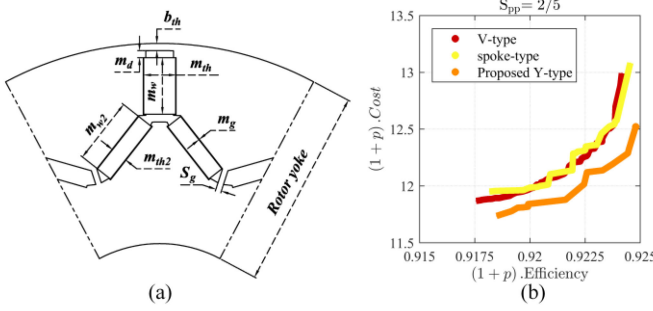


Fig. 9. (a) The cross-sections and geometric parameters of the novel Y-type rotor topology and (b) Pareto-front of the three designs.

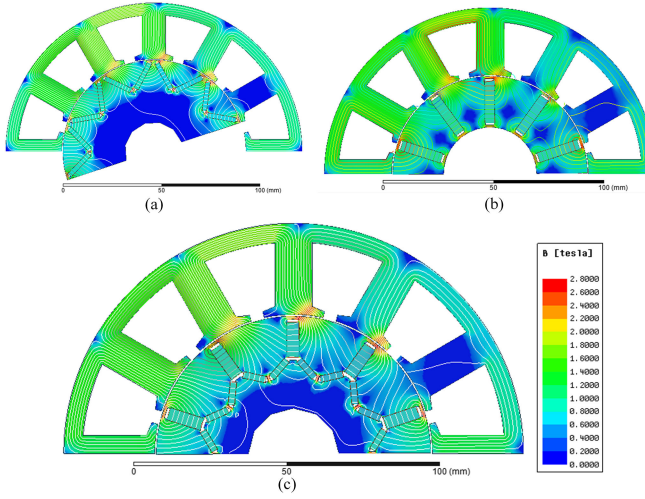


Fig. 10. Distribution of flux density and flux lines at rated speed and current (a) V-type, (b) Spoke-type, and (c) Y-type at the initial rotor position.

could be developed. The novel rotor referred hereafter as Y-type should maximize the torque density and minimize the torque ripple simultaneously. A Y-type rotor was optimized using the same procedure described before in Section III to validate these theoretical assumptions.

The Fig. 9(a) shows the geometrical parameters of the proposed Y-type rotor. The geometry was parameterized in a way so that all three types of rotors can be obtained with minimum geometrical changes. For example, the spoke section could be increased to a maximum value, which will result in a spoke-type rotor. Such a parameterization will help to find the optimum proportion of spoke and V-section for the Y-type rotor. In the Y-configuration, the spoke section is closer to airgap and away from the shaft. The V-section at the bottom of spoke-section prevents magnet fluxes of spoke-type from shortening at the thin iron bridges above the shaft (as seen in Fig. 10(b)) resulting in better airgap flux linkage to aid in improving torque density.

The Pareto front of Fig. 8(a) and (b) were obtained from the multiobjective optimization described in Section III without giving consideration to violation of design constraints. These Pareto fronts were tightened up by applying a penalty factor p to the design candidates that violate any of the constraints of

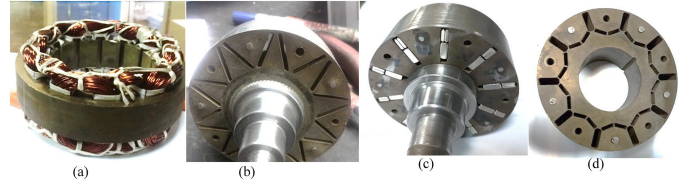


Fig. 11. (a) The FSCW stator and the 3 prototype rotors (b) V-type, (c) Spoke-type, and (d) Y-type.

Table III. The penalty factor is defined as below:

$$\begin{cases} (1+p) \cdot \text{Cost} \\ (1+p) \cdot \text{Efficiency} \end{cases}, \text{ for } p = \sum_i w_i (C_i - C_{ni}) \quad (12)$$

where w_i is the weighted factor for each constraint, C_i is the value of i th constraint, and C_{ni} is the nominal value of i th constraint.

Fig. 9(b) compares the Pareto fronts of the three topologies, in which the design candidates were determined after the constraint penalty was applied, and designs that violate constraints were excluded. Thus, all the design candidates of the Pareto-front of Fig. 9(b) satisfy the torque ripple constraints of $<5\%$.

Three final candidates were selected from the Pareto fronts of Fig. 9(b) for performance comparison and experimental verification using post-optimization selection criteria. As a first-step of the selection criteria, even tighter restriction were applied to the constraints and objectives (cost $<\$15$, efficiency >0.91 , saliency ratio >1.2 , characteristic current $<1.05\text{pu}$, flux density of stator tooth $<1.6\text{T}$ and THD of voltage $<5\%$). A set of designs which do not violate these tighter boundaries were identified and separated in a set. The mean value of each design variable in the set was considered as the optimized value of a variable of the nominated design. The three final candidates, thus selected, were manufactured as the prototype designs.

VI. COMPARISON AND EXPERIMENTAL VALIDATION

The flux distributions of the three optimized designs are shown in Fig 10. The magnetic saturation levels of the three designs are similar. However, the distributions of the flux lines are very different in three machines as expected.

Three prototypes were constructed based on the optimized designs. The stator and the rotors are shown in Fig. 11. Each of the prototypes was run under various operating conditions using the same test set-up. The back EMF of each prototype was measured when they were turned at various speed by a servo motor acting as a prime mover. Fig. 12 compares the measured back EMF waveforms (line-neutral) of the three prototypes. The Y-type prototype has the highest amplitude, and all three waveforms are fairly sinusoidal with a small third harmonic component.

From the fundamental of the back EMF, the magnet flux linkage λ_{pmd} was found. The magnet flux linkage λ_{pmd} of the Y-type prototype is 9.6% and 22.4% higher than the V-type and spoke-type, respectively, as shown in Table V.

The cogging torque was measured using a high-resolution torque transducer at various rotor positions when the rotor was locked at these positions. The incremental step for each position

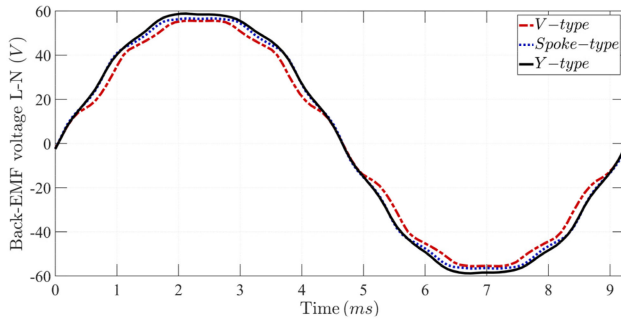


Fig. 12. The measure phase back EMF waveforms of the three prototypes when running at 1300 rpm.

TABLE V
COMPARISON OF MACHINE PARAMETERS

Parameters	V-type	Spoke-type	Y-type
Magnet flux linkage λ_{pm} [Wb]	0.0897	0.0804	0.0984
d-axis inductance L_d [mH]	9.37	10.45	9.50
q-axis inductance L_q [mH]	12.75	14	12.8
Saliency	1.36	1.33	1.35

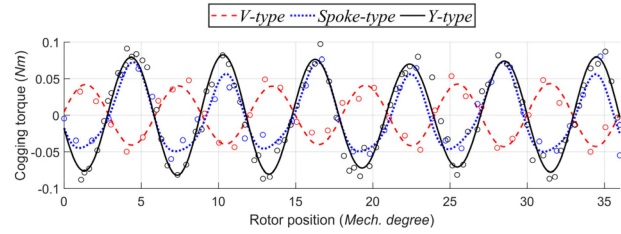


Fig. 13. Comparison of measured cogging torque waveforms of the three prototypes. ‘o’ are measured static torque points which were curve fitted as the waveform.

was selected considering the cycles in cogging torque waveform in one mechanical revolution. The LCM of the 12-slot/10-pole combination is 60, and hence, there are 60 cycles of cogging torque in 360(mech). A step of 1(mech) is appropriate for the measurement. Fig. 13 compares the cogging torque measured for one pole-pitch of the three prototypes. The peak cogging torque of the V-type rotor is the lowest, and the cogging torque waveforms of spoke-type and Y-type are in a phase opposite to V-type as seen in Fig. 13. Thus, the rotor position at which the cogging torque of the V-type has its positive peak the spoke- and Y-type have their negative peak of the cogging torque. As a result, the peaks of cogging torque of the Y- and spoke-type have the opposite effect on the overall torque ripple compared to the V-type. It was found that if the spoke-type magnet pole locates at the q -axis of the V-type, the peaks of the two cogging torque waveforms occur at the phase opposite. The positive peak of the cogging torque of the V-type rotor adds on the resulting torque ripple. Since, in case of the spoke-type, it is the negative peak of the cogging torque, it gets subtracted from the overall torque ripple resulting in a reduced amplitude. A detailed study carried out in [46] reveals that along with cogging torque, ripples caused by cross-magnetization due to localized magnetic saturation also

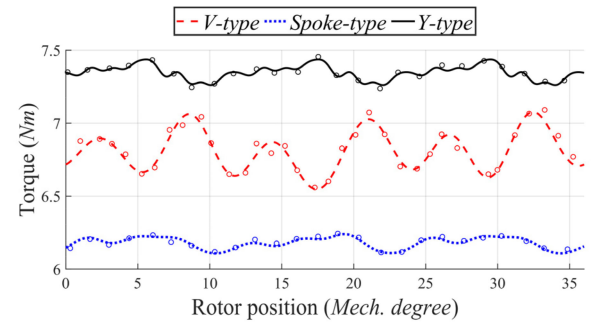


Fig. 14. Comparison of measured torque ripple of three prototypes.

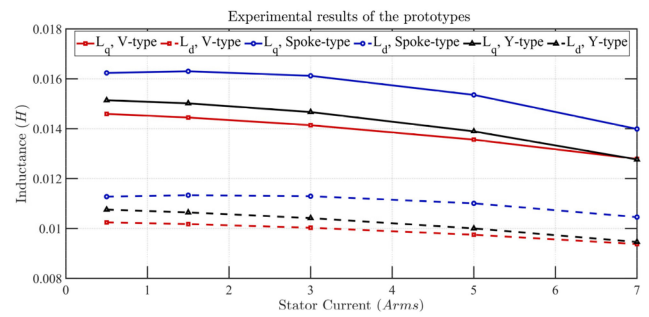


Fig. 15. Measured variation of L_d , L_q inductances of the three prototypes.

plays a significant role in reducing the torque ripple in the FSCW spoke-type IPMSM. Thus, in the Y-type configuration by maintaining the position of the spoke-part at the q -axis of V-section, the overall torque ripple could be minimized.

The comparison of the measured overall torque ripple of the three prototypes in Fig. 14 shows that Y-type has the lowest torque ripple. It can also be seen from Fig. 14 that the average torque of Y-type is 18.9% and 7.7% higher than that of the spoke- and V-type respectively. This comparison confirms the highest torque density and the lowest torque ripple of the Y-type motor compared to the other two.

To assess the effect of saturation on the parameters, the variation of d - and q -axis inductances L_d and L_q of the three prototypes for varying currents were measured and shown in Fig. 15. The variations of L_d and L_q for all three motors are similar with minimal reduction with increasing current. L_d and L_q and saliency ratios at the rated current are given in Table V. The saliencies of the V- and Y-type are higher than the spoke-type.

To analyze the steady-state performances of the three prototypes, they were run in the full operating range under full load using conventional field-oriented control. The torque-speed and the power-speed characteristics were measured and compared in Fig. 16. Efficiencies under various operating conditions were also measured using standard efficiency measurement method and compared in Fig. 17. MTPA trajectory control was used at constant torque region up to base speed, and above this speed, the flux-weakening algorithm was employed to maintain the rated voltage. It can be seen from Figs. 16 and 17 that Y-type FSCW IPMSM outperforms other two in the entire operating range.

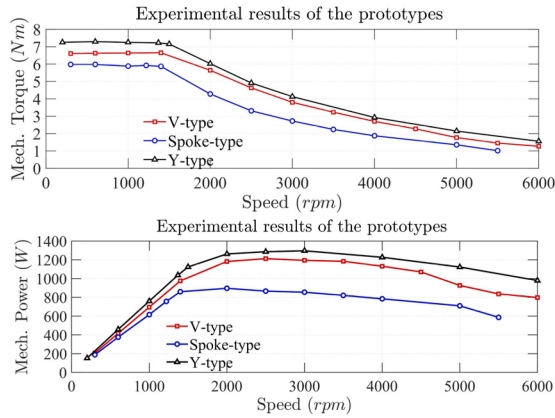


Fig. 16. Comparison of measured torque and power-speed characteristics of the 3 prototypes.

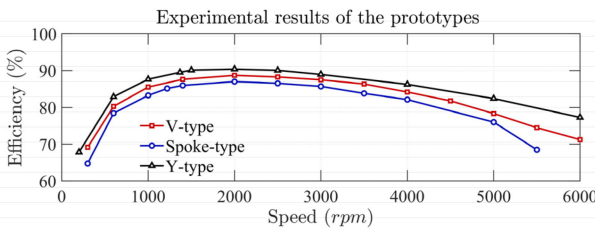


Fig. 17. Comparison of measured efficiency of the three prototypes.

TABLE VI
PERFORMANCE SUMMARY OF A SCALED-UP Y-TYPE ROTOR

Parameter	Target	FSCW Y-type motor
Rated power	30kW	✓
Peak power	55kW for 18 s	✓
Maximum speed	14000 rpm	✓
Efficiency	>95%	✓
Machine volume	<9.7L	4.78L
Maximum back EMF at maximum speed	<600V	550V
Torque ripple	<5%	3.3%

Also, the Y-type FSCW IPMSM reaches a CPSR of 1:4.5, which is 36% higher than the CPSR of the V- and spoke-type.

The performance study of a scaled-up version of the Y-type motor (peak power 55kW for 18s, 30kW continuous) was also carried out to evaluate the potential of the Y-type IPMSM for electric vehicle applications. The predicted torque-speed performance of this proposed motor is compared with the target characteristic of Freedomcar 2020 in Fig. 18(a). The efficiency of this scaled-up Y-type motor in full-speed range was compared against the Toyota Prius IPMSM (2010) in Fig. 18(b) to give a perspective. Table VI summarizes other key performances of the proposed motor in terms of Freedomcar 2020 targets. The comparison study of the proposed Y-type IPMSM thus shows excellent potential for applications similar to EV traction drive.

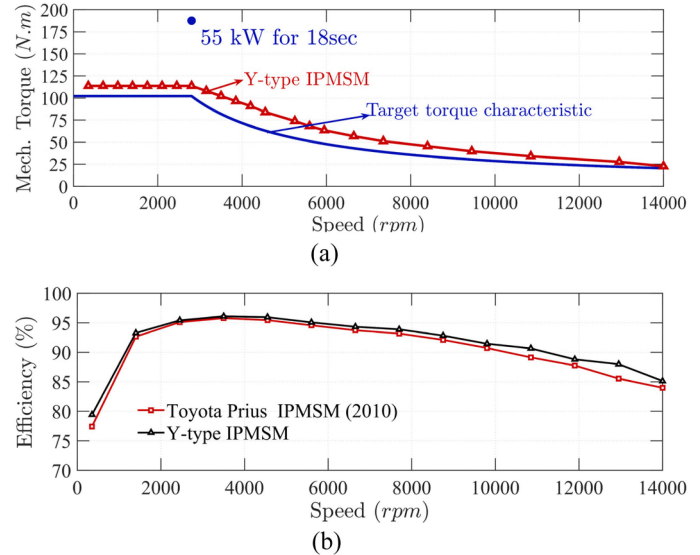


Fig. 18. Compares scaled-up Y-type IPMSM (a) torque-speed characteristic with Freedomcar 2020 target (b) efficiency of the full speed range with Toyota Prius IPMSM (2010).

VII. CONCLUSION

A multiobjective optimization technique was developed based on NSGA-II and transient CE-FEA for FSCW IPMSMs. The accuracy of estimating MTPA trajectory, characteristic current and saliency ratio during the optimization was significantly improved by including the effect of magnetic saturation. It was achieved without a substantial increase in computational time. The technique was used to optimize a V-type and a spoke-type FSCW IPMSM for high torque density and low torque ripple. A detailed comparison of performances reveals that two topologies can be combined to a new rotor topology named as Y-type, which provide a possibility to minimize torque ripple without sacrificing torque density.

The extensive experimental verification confirms that the proposed Y-type motor has higher torque density, lower torque ripple, higher efficiency and wider CPSR capability than both the V- and spoke-type FSCW IPMSM. The spoke section of the Y-type rotor ensures low torque ripple, whereas, the V-section increases the torque density by improving the flux concentration and reluctance torque. Thus, in the Y-type motor, the torque ripple could be decreased without sacrificing torque density. As the Y-type rotor combines the goodness of both spoke and V-type, and at the same time provides more flexibility in the rotor design.

REFERENCES

- [1] B. P. Rocadio, "Design and analysis of fractional-slot concentrated-winding multiphase fault-tolerant permanent magnet synchronous machines," Ph.D. dissertation, Dept. Elect. Mach. Elect. Circuits, Tecnum School of Eng., Universidad de Navarra, 2015.
- [2] P. Waide and C. U. Brunner, "Energy-efficiency policy opportunities for electric motor-driven systems," 2011. [Online]. Available: <https://doi.org/10.1787/5kgg52gb9gjd-en>

- [3] N. Bianchi, S. Bolognani, M. D. Pre, and G. Grezzani, "Design considerations for fractional-slot winding configurations of synchronous machines," *IEEE Trans. Ind. Appl.*, vol. 42, no. 4, pp. 997–1006, Jul./Aug. 2006.
- [4] A. G. Jack, B. C. Mecrow, and J. A. Haylock, "A comparative study of permanent magnet and switched reluctance motors for high-performance fault-tolerant applications," *IEEE Trans. Ind. Appl.*, vol. 32, no. 4, pp. 889–895, Jul./Aug. 1996.
- [5] A. M. El-Refaie, "Fractional-slot concentrated-windings synchronous permanent magnet machines: Opportunities and challenges," *IEEE Trans. Ind. Electron.*, vol. 57, no. 1, pp. 107–121, Jan. 2010.
- [6] R. Dutta, L. Chong, and M. F. Rahman, "Design and experimental verification of an 18-slot/14-pole fractional-slot concentrated winding interior permanent magnet machine," *IEEE Trans. Energy Convers.*, vol. 28, no. 1, pp. 181–190, Mar. 2013.
- [7] S. Chung, J. Kim, Y. Chun, B. Woo, and D. Hong, "Fractional slot concentrated winding PMSM with consequent pole rotor for a low-speed direct drive: Reduction of rare earth permanent magnet," *IEEE Trans. Energy Convers.*, vol. 30, no. 1, pp. 103–109, Mar. 2015.
- [8] A. Tessarolo, C. Ciriani, M. Bortolozzi, M. Mezzarobba, and N. Barbini, "Investigation into multi-layer fractional-slot concentrated windings with unconventional slot-pole combinations," *IEEE Trans. Energy Convers.*, vol. 34, no. 4, pp. 1985–1996, Dec. 2019.
- [9] P. B. Reddy, A. M. El-Refaie, K. Huh, J. K. Tangudu, and T. M. Jahns, "Comparison of interior and surface PM machines equipped with fractional-slot concentrated windings for hybrid traction applications," *IEEE Trans. Energy Convers.*, vol. 27, no. 3, pp. 593–602, 2012.
- [10] P. Asef, R. B. Perpiñà, S. Moazami, and A. C. Lapthorn, "Rotor shape multi-level design optimization for double-stator permanent magnet synchronous motors," *IEEE Trans. Energy Convers.*, vol. 34, no. 3, pp. 1223–1231, Sep. 2019.
- [11] H. Dhulipati, E. Ghosh, S. Mukundan, P. Korta, J. Tjong, and N. C. Kar, "Advanced design optimization technique for torque profile improvement in six-phase PMSM using supervised machine learning for direct-drive EV," *IEEE Trans. Energy Convers.*, vol. 34, no. 4, pp. 2041–2051, Dec. 2019.
- [12] P. Asef, R. B. Perpiñà, M. R. Barzegaran, A. Lapthorn, and D. Mewes, "Multiobjective design optimization using dual-level response surface methodology and Booth's algorithm for permanent magnet synchronous generators," *IEEE Trans. Energy Convers.*, vol. 33, no. 2, pp. 652–659, Jun. 2018.
- [13] K. Ahsanullah, R. Dutta, and M. F. Rahman, "Analysis of low-speed IPMMs with distributed and fractional slot concentrated windings for wind energy applications," *IEEE Trans. Magn.*, vol. 53, no. 11, pp. 1–10, 2017.
- [14] J. K. Tangudu, T. M. Jahns, and A. El-Refaie, "Unsaturated and saturated saliency trends in fractional-slot concentrated-winding interior permanent magnet machines," in *Proc. Energy Convers. Congr. Expo.*, Sep. 2010, pp. 1082–1089.
- [15] E. Carraro, N. Bianchi, S. Zhang, and M. Koch, "Design and performance comparison of fractional slot concentrated winding spoke type synchronous motors with different slot-pole combinations," *IEEE Trans. Ind. Appl.*, vol. 54, no. 3, pp. 2276–2284, May/Jun. 2018.
- [16] C. Shi-Uk, K. Jong-Moo, K. Dae-Hyun, W. Byung-Chul, H. Do-Kwan, and L. Ji-Young, "Fractional slot concentrated winding permanent magnet synchronous machine with consequent pole rotor for low speed direct drive," *IEEE Trans. Magn.*, vol. 48, no. 11, pp. 2965–2968, 2012.
- [17] P. Ponomarev, P. Lindh, and J. Pyrhönen, "Effect of slot-and-pole combination on the leakage inductance and the performance of tooth-coil permanent-magnet synchronous machines," *IEEE Trans. Ind. Electron.*, vol. 60, no. 10, pp. 4310–4317, Oct. 2013.
- [18] J. Cros and P. Viarouge, "Synthesis of high performance PM motors with concentrated windings," *IEEE Trans. Energy Convers.*, vol. 17, no. 2, pp. 248–253, 2002.
- [19] D. Wu and Z. Q. Zhu, "Influence of slot and pole number combinations on voltage distortion in surface-mounted permanent magnet machines with local magnetic saturation," *IEEE Trans. Energy Convers.*, vol. 30, no. 4, pp. 1460–1471, Dec. 2015.
- [20] N. Bianchi and E. Fornasiero, "Impact of MMF space harmonic on rotor losses in fractional-slot permanent-magnet machines," *IEEE Trans. Energy Convers.*, vol. 24, no. 2, pp. 323–328, Jun. 2009.
- [21] P. B. Reddy, A. M. El-Refaie, and K. Huh, "Effect of number of layers on performance of fractional-slot concentrated-windings interior permanent magnet machines," *IEEE Trans. Power Electron.*, vol. 30, no. 4, pp. 2205–2218, Apr. 2015.
- [22] K. Wang, Z. Q. Zhu, and G. Ombach, "Synthesis of high performance fractional-slot permanent-magnet machines with coil-pitch of two slot-pitches," *IEEE Trans. Energy Convers.*, vol. 29, no. 3, pp. 758–770, Sep. 2014.
- [23] I. Petrov, P. Ponomarev, Y. Alexandrova, and J. Pyrhönen, "Unequal teeth widths for torque ripple reduction in permanent magnet synchronous machines with fractional-slot non-overlapping windings," *IEEE Trans. Magn.*, vol. 51, no. 2, pp. 1–9, 2015.
- [24] X. Zhu, W. Wu, L. Quan, Z. Xiang, and W. Gu, "Design and multi-objective stratified optimization of a less-rare-earth hybrid permanent magnets motor with high torque density and low cost," *IEEE Trans. Energy Convers.*, vol. 34, no. 3, pp. 1178–1189, Sep. 2019.
- [25] A. Pouramin, R. Dutta, and M. F. Rahman, "Preliminary study on differences in the performance characteristics of concentrated and distributed winding IPM machines with different rotor topologies," in *Proc. IEEE Energy Convers. Congr. Expo.*, Oct. 2017, pp. 3565–3570.
- [26] A. Walker, M. Galea, D. Gerada, C. Gerada, A. Mebareki, and N. Brown, "Development and design of a high performance traction machine for the FreedomCar 2020 traction machine targets," in *Proc. XXII Int. Conf. Elect. Mach.*, Sep. 2016, pp. 1611–1617.
- [27] N. Bianchi, M. Pré, L. Alberti, and E. Fornasiero, "Theory and design of fractional-slot PM machines, ser," *IEEE IAS Tutorial Course notes, IAS*, vol. 7, 2007.
- [28] A. El-Refaie, "Fractional-slot concentrated-windings: A paradigm shift in electrical machines," in *Proc. IEEE Elect. Mach. Des. Control Diagnosis Workshop*, Mar. 2013, pp. 24–32.
- [29] L. Chong, R. Dutta, and M. F. Rahman, "A comparative study of rotor losses in an IPM with single and double layer concentrated windings," in *Proc. Elect. Mach. Syst., Int. Conf.*, Oct. 2010, pp. 942–946.
- [30] N. Bianchi, S. Bolognani, X. Pre, M. D., and G. Grezzani, "Design considerations for fractional-slot winding configurations of synchronous machines," *IEEE Trans. Ind. Appl.*, vol. 42, no. 4, pp. 997–1006, 2006.
- [31] L. Alberti and N. Bianchi, "Theory and design of fractional-slot multilayer windings," *IEEE Trans. Ind. Appl.*, vol. 49, no. 2, pp. 841–849, 2013.
- [32] E. Fornasiero, L. Alberti, N. Bianchi, and S. Bolognani, "Considerations on selecting fractional-slot nonoverlapped coil windings," *IEEE Trans. Ind. Appl.*, vol. 49, no. 3, pp. 1316–1324, 2013.
- [33] N. Bianchi and M. Dai Pre, "Use of the star of slots in designing fractional-slot single-layer synchronous motors," *Elect. Power Appl., IEE Proc.*, vol. 153, no. 3, pp. 459–466, 2006.
- [34] D. Yao and D. M. Ionel, "A review of recent developments in electrical machine design optimization methods with a permanent-magnet synchronous motor benchmark study," *IEEE Trans. Ind. Appl.*, vol. 49, no. 3, pp. 1268–1275, 2013.
- [35] K. Deb, A. Pratap, S. Agarwal, and T. Meyarivan, "A fast and elitist multi-objective genetic algorithm: NSGA-II," *IEEE Trans. Evol. Computation*, vol. 6, no. 2, pp. 182–197, Apr. 2002.
- [36] A. Pouraminiain, "Design optimization of high-performance interior permanent magnet machines using a fast and accurate FE-based technique," PhD, Univ. New South Wales (UNSW Sydney), 2019.
- [37] N. Srinivas and K. Deb, "Multiobjective optimization using nondominated sorting in genetic algorithms," *Evol. Comput.*, vol. 2, no. 3, pp. 221–248, 1994.
- [38] D. M. Ionel and M. Popescu, "Ultrafast finite-element analysis of brushless PM machines based on space-time transformations," *IEEE Trans. Ind. Appl.*, vol. 47, no. 2, pp. 744–753, 2011.
- [39] G. Y. Sizov, D. M. Ionel, and N. A. O. Demerdash, "Modeling and parametric design of permanent-magnet AC machines using computationally efficient finite-element analysis," *IEEE Trans. Ind. Electron.*, vol. 59, no. 6, pp. 2403–2413, 2012.
- [40] A. Pouramin, R. Dutta, M. F. Rahman, and D. Xiao, "Inductances of a fractional-slot concentrated-winding interior PM synchronous machine considering effects of saturation and cross magnetization," in *Proc. Energy Convers. Congr. IEEE*, Sep. 2015, pp. 6075–6081.
- [41] A. M. El-Refaie and T. M. Jahns, "Optimal flux weakening in surface PM machines using fractional-slot concentrated windings," *IEEE Trans. Ind. Appl.*, vol. 41, no. 3, pp. 790–800, 2005.
- [42] D. M. Ionel and M. Popescu, "Finite-element surrogate model for electric machines with revolving field-application to IPM motors," *IEEE Trans. Ind. Appl.*, vol. 46, no. 6, pp. 2424–2433, 2010, doi: [10.1109/TIA.2010.2073671](https://doi.org/10.1109/TIA.2010.2073671).
- [43] Z. Peng *et al.*, "Multi-objective tradeoffs in the design optimization of a brushless permanent-magnet machine with fractional-slot concentrated windings," *IEEE Trans. Ind. Appl.*, vol. 50, no. 5, pp. 3285–3294, 2014.

- [44] A. Fatemi, N. A. O. Demerdash, T. W. Nehl, and D. M. Ionel, "Large-scale design optimization of pm machines over a target operating cycle," *IEEE Trans. Ind. Appl.*, vol. 52, no. 5, pp. 3772–3782, 2016.
- [45] K. Liu, Q. Zhang, J. Chen, Q. Zhu, J. Zhang, and A. Shen, "Online multi-parameter estimation of non-salient pole PM synchronous machines with temperature variation tracking," *IEEE Trans. Ind. Electron.*, vol. PP, no. 99, pp. 1–1, 2010.
- [46] G. Chu, R. Dutta, A. Pouramin, and M. F. Rahman, "Analysis of torque ripple of a spoke-type interior permanent magnet machine," *Energies*, vol. 13, no. 11, 2020, Art. no. 2886.



Rukmi Dutta (Senior Member, IEEE) received the bachelor's of engineering degree from Assam Engineering College, Guwahati University, India, 1996 and the Ph.D. degree from the UNSW Sydney, Australia, in 2007, both in electrical engineering.

She is currently an Associate Professor with UNSW Sydney. Prior to this, she was an Electrical Engineer with CMG Pty Ltd (currently Regal Beloit Australia) and as an Associate Lecturer with UNSW, Australia. She was also briefly with the Institute of Industrial Science, Tokyo University, Japan, and Reliance Industry Ltd, India. Her research interests include permanent magnet machine design and control, electromagnetic analysis of electric devices, renewable energy, and distributed generation.



Alireza Pouramin received the B.Sc. and M.Sc. degrees in electrical engineering from the Isfahan University of Technology, Isfahan, Iran, in 2005 and 2009, respectively, and the Ph.D. degree in electrical engineering from the UNSW Sydney, Australia, in 2019. He was former Research Associate in Energy Systems with the School of Electrical Engineering, University of New South Wales, Sydney.

His research interests include permanent magnet machine and induction machine design, multiobjective optimization algorithms, high-speed electric motors, and power system transient analysis.



Muhammed F. Rahman (Life Fellow, IEEE) received the B.E. (Hons.) degree in electrical engineering from the Bangladesh University of Engineering and Technology, Dhaka, in 1972, and the M.Sc. and Ph.D. degrees from University of Manchester Institute of Science and Technology, U.K., in 1975 and 1978, respectively. He subsequently was a Systems Design Engineer with the General Electric Company, Rugby, U.K., for two years before joining the National University of Singapore in 1980 as a Lecturer. He is currently a Professor in Energy Systems with the School of Electrical Engineering, University of New South Wales, Sydney, Australia. His research interests include power electronics, electric drives, electrical machines, and motion control systems.